arXiv:hep-ph/0403022v1 2 Mar 2004

Microscopic description of anisotropic flow in relativistic heavy ion collisions

E. Zabrodin[a,c,d], L. Bravina[b,d], C. Fuchs[a], A. Faessler[a]

[a] *Institute for Theoretical Physics, University of Tübingen, D-72076 Tübingen, Germany*
[b] *Department of Physics, University of Oslo, N-0316 Oslo, Norway*
[c] *Centre of Mathematics for Applications, University of Oslo, N-0316 Oslo, Norway*
[d] *Institute for Nuclear Physics, Moscow State University, RU-119899 Moscow, Russia*

Abstract. Anisotropic flow of hadrons is studied in heavy ion collisions at SPS and RHIC energies within the microscopic quark-gluon string model. The model was found to reproduce correctly many of the flow features, e.g., the wiggle structure of direct flow of nucleons at midrapidity, or centrality, rapidity, and transverse momentum dependences of elliptic flow. Further predictions are made. The differences in the development of the anisotropic flow components are linked to the freeze-out conditions, which are quite different for baryons and mesons.

1. INTRODUCTION

The study of properties of extremely hot and dense nuclear matter, and the search for anticipated transition to a deconfined phase of quarks and gluons, the so-called Quark-Gluon Plasma (QGP), is one of the main objectives of heavy ion experiments at ultra-relativistic energies. Both theorists and experimentalists are looking for genuine QGP fingerprints, that cannot be masked or washed out by processes on a hadronic level. At present, the expansion of highly compressed nuclear mater in the direction perpendicular to the beam axis of the colliding heavy ions, known as collective flow, is believed to be one of the most promising signals to detect the creation of the QGP [1,2,3]. Since the development of flow is closely related to the equation of state (EOS) of nuclear matter, the investigation of the flow can shed light on the transition to the QGP phase accompanied by its subsequent hadronization [4,5,6,7,8,9,10,11,12,13,14,15,16,17,18,19]. If the transition from the QGP to hadronic phase is of first order, the vanishing of the pressure gradients in the mixed phase leads to the so-called softening of the EOS [6,7]. The latter should be distinctly seen in the behavior of the excitation function of the collective flow. This circumstance explains the great interest in the transverse flow phenomenon.

The Fourier expansion technique is usually employed to study collective flow phenomena since [20,21]. The invariant distribution Ed^3N/d^3p is presented as

$$E\frac{d^3N}{d^3p} = \frac{1}{\pi}\frac{d^2N}{dp_t^2dy}\left[1 + 2\sum_{n=1}^{\infty} v_n \cos(n\phi)\right], \tag{1}$$

where p_t and y are the transverse momentum and the rapidity, and ϕ is the azimuthal angle between the momentum of the particle and the reaction plane. The first two Fourier

coefficients in Eq. (1), v_1 and v_2, are dubbed directed flow and elliptic flow, respectively. Since both types of anisotropic flow depend on rapidity y, transverse momentum p_t, and the impact parameter of an event b (i.e., $v_n \equiv v_n(x_j)$, where $\{x_{j=1,2,3}\} \equiv \{y, p_t, b\}$), the following differential distributions are usually applied

$$v_n(x_i, \Delta x_{j\neq i}) = \int_{x_j^{(1)}}^{x_j^{(2)}} \cos(n\phi) \frac{d^3N}{d^3x_j} d^2x_{j\neq i} \Big/ \int_{x_j^{(1)}}^{x_j^{(2)}} \frac{d^3N}{d^3x_j} d^2x_{j\neq i} \ . \tag{2}$$

Model calculations suggest that elliptic flow is built up at the early phase of nuclear collisions [10,14,15], whereas directed flow develops until the late stage of the reaction [22, 23,24]. But it is well known that the particles with high transverse momentum are emitted at the onset of the collective expansion, i.e., their directed flow can carry information about the EOS of the dense nuclear phase. The study of the collective flow development is, therefore, closely connected to the freeze-out picture. In this article the microscopic quark-gluon string model (QGSM) [25,26] is employed to investigate the formation and evolution of anisotropic flow components in heavy ion collisions at SPS ($\sqrt{s} = 17.8$ AGeV) and RHIC ($\sqrt{s} = 130$ and 200 AGeV) energies. Note that QGSM does not implement the formation of a QGP at the early stage of the collision. Our goal is to understand to what extent the characteristic signals of the hot nuclear matter can be reproduced. A noticeable discrepancy between experimental data and QGSM predictions being observed, this should be considered as an indication for new processes not included in the model.

2. MODEL

The QGSM is based on the $1/N_c$ (where N_c is the number of quark colors or flavors) topological expansion of the amplitude for processes in quantum chromodynamics and string phenomenology of particle production in inelastic binary collisions of hadrons. The diagrams of various topology, which arose due to the $1/N_c$ expansion, correspond at high energies to processes with exchange of Regge singularities in the t-channel. For instance, planar and cylindrical diagrams corresponds to the Reggeon and Pomeron exchange, respectively. The QGSM treats the elementary hadronic interactions on the basis of the Gribov-Regge theory (GRT), similar to the dual parton model [27] and the VENUS model [28]. This implies the consideration of subprocesses with quark annihilation and quark exchange, corresponding to Reggeon exchanges in two-particle amplitudes in the GRT, and with color exchange, corresponding to the one and more Pomeron exchanges in elastic amplitudes. The hh collision term includes also single and double diffraction subprocesses, antibaryon-baryon annihilation and elastic scattering, as well as the hard gluon-gluon scattering with large $Q^2 > 1$ (GeV/c)^2 momentum transfer [29].

The inelastic hh cross section $\sigma_{in}(s)$ can be calculated via the real part of the eikonal

$$\sigma_{in}(s) = 2\pi \int_0^\infty \left\{1 - \exp\left[-2u^R(s,b)\right]\right\} bdb \ . \tag{3}$$

Here s is the center-of-mass energy of the reaction. The eikonal $u(s,b)$ can be presented as a sum of three terms corresponding to soft and hard Pomeron exchange, and triple Pomeron exchange, which is responsible for the single diffraction process,

$$u^R(s,b) = u^R_{soft}(s,b) + u^R_{hard}(s,b) + u^R_{triple}(s,b) \ . \tag{4}$$

Using the Abramovskii-Gribov-Kancheli (AGK) cutting rules [30] the inelastic cross section of hh interaction can be presented as

$$\sigma_{in}(s) = \sum_{i,j,k=0;i+j+k\geq 1} \sigma_{ijk}(s) \ , \tag{5}$$

$$\sigma_{ijk}(s) = 2\pi \int_0^\infty bdb \exp\left[-2u^R(s,b)\right] \frac{\left[2u^R_{soft}(s,b)\right]^i}{i!} \frac{\left[2u^R_{hard}(s,b)\right]^j}{j!} \frac{\left[2u^R_{triple}(s,b)\right]^k}{k!} \ . \tag{6}$$

The last equation enables one to determine the number of cut soft and hard Pomerons, i.e., the number of strings and hard jets. The single Pomeron exchange leads to the formation of two quark-diquark or quark-antiquark strings. With rising energy the processes with multi-Pomeron exchanges become more and more important. The contribution of the cylinder diagrams to the scattering amplitude increases like $s^{\alpha_P(0)-1}$, while that of the so-called chain diagrams corresponding to n-Pomeron exchanges ($n \geq 2$) rises like $s^{n[\alpha_P(0)-1]}$ with $\alpha_P(0) > 1$ being the intercept of a Pomeranchuk pole. Strings, which are formed in the course of a hh or A+A collision, decay later into secondary hadrons. Similar to hadronic collisions, string fragmentation into hadrons proceeds independently in A+A collision also. However, in the latter case these hadrons are allowed to interact with other hadrons after a certain formation time, while the valence quarks and diquarks can interact promptly with the reduced cross sections. The model simplifies the nuclear effects and concentrates on hadron rescattering. As independent degrees of freedom QGSM includes octet and nonet vector and pseudoscalar mesons, and octet and decuplet baryons, and their antiparticles.

The transverse motion of hadrons in the QGSM arises from different sources: (i) primordial transverse momentum of the constituent quarks, (ii) transverse momentum of (di)quark-anti(di)quark pairs acquired at string breakup, (iii) the transverse Fermi motion of nucleons in colliding nuclei, and (iv) rescattering of secondaries. Parameters of the first two sources are fixed by comparison with hadronic data. The Fermi motion changes the effective transverse distribution of strings formed by the valence quarks and diquarks of the target and projectile nucleons. Thus, the original strings are not completely parallel to the beam axis. Further details of the QGSM can be found elsewhere [25,26]. We start from the study of energy and centrality dependence of the directed flow.

3. DIRECTED FLOW

The directed flow of nucleons at BEVALAC/SIS energies ($E_{lab} = 0.1$ AGeV - 1 AGeV) and at AGS energy ($E_{lab} = 10.7$ AGeV) has a characteristic S-shape attributed to the standard $\langle p_x/A \rangle$ distribution. It grows linearly with rising rapidity between the target and projectile fragmentation regions. Conventionally, we will call this type of flow, for which the slope dv_1/dy_{cm} is positive, *normal* flow, in contrast to the *antiflow* for which $dv_1/dy_{cm} < 0$ in the midrapidity region.

The one-fluid hydrodynamic models indicate that deviations from the straight line behavior of the nucleon flow can be caused solely by the softening of the EOS due to the QGP creation [12]. In microscopic string model calculations such deviations were first observed in very peripheral Au+Au collisions at AGS energy [9]. It appeared, however, that

the effect is shifted to more central topologies [23,24] as the collision energy increases. The phenomenon leading to the formation of a characteristic *wiggle* structure [31] of the directed flow is caused by shadowing, which plays a decisive role in the competition between normal flow and antiflow in noncentral nuclear collisions at ultrarelativistic energies.

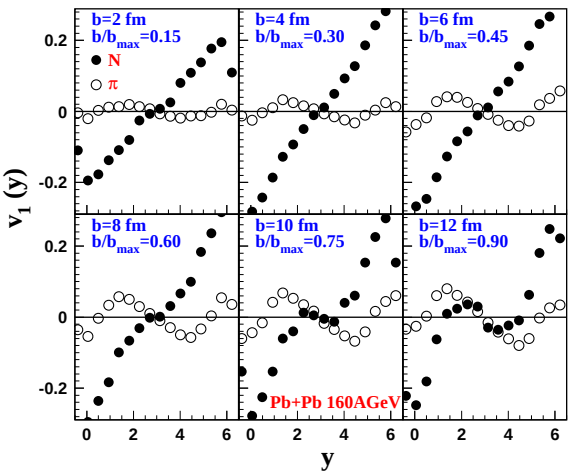

Figure 1. Directed flow of nucleons (full circles) and pions (open circles) as a function of rapidity in lead-lead collisions at 160 AGeV.

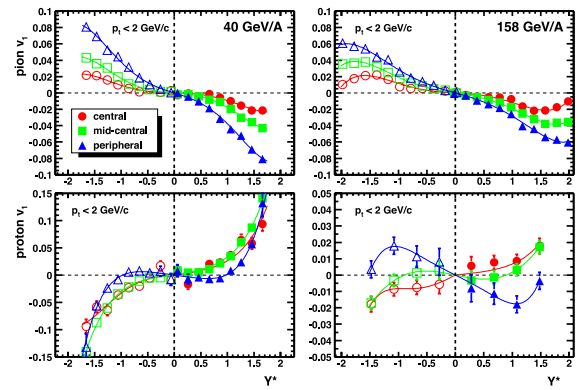

Figure 2. Directed flow of protons and pions in Pb+Pb collisions at 40 AGeV and 160 AGeV measured by NA49 Collaboration [32].

Hadrons, emitted with small rapidities in the antiflow area, can propagate freely, while their counterparts will be absorbed by dense baryon-rich matter. The rapidity dependence of the directed flow of nucleons and pions in Pb+Pb at SPS is presented in Fig. 1 for six different impact parameters. Here deviations from the straight line start to develop at $b/b_{max} = 0.45$ in the central rapidity window. Recently, the wiggle structure of directed flow of protons in peripheral lead-lead collisions at SPS has been observed by NA49 Collaboration [32] (see Fig. 2). This result cannot be explained by the effective softening of the EOS in microscopic models due to production of strongly interacting string matter, because the number of the strings is significantly reduced as the collisions become more peripheral. In hydrodynamics, even if the tilted region is non-perpendicular to the beam axis [17], the tendency should be opposite: Here the antiflow reaches its maximum strength in semicentral events and almost disappear in peripheral ones.

Our next step is to study the time development of the directed flow of strange hadrons, primarily, kaons and antikaons, in order to check the role of baryon-antibaryon asymmetry. For instance, K^- and $\overline{K}^0$ can be absorbed via the channels such as $K^- + p \to \Lambda + \pi^+$, etc., whereas there are no analogous reactions for K^+ and K^0. How important is this reaction asymmetry at SPS and, especially, at RHIC energies, where the matter is expected to be meson-dominated? These problems have been addressed in [33].

The time evolution of directed flow of kaons and antikaons in minimum bias Pb+Pb collisions at 160 AGeV is presented in Fig. 3. Here the coefficient $v_1^K(y)$ is calculated in different transverse momentum intervals at early, $t = 3$ fm/c and $t = 10$ fm/c, and the final stage of the reaction, $t \geq 60$ fm/c. To avoid ambiguities, all resonances in the scenario with early freeze-out were allowed to decay according to their branching ratios. The flow evolution is seen quite distinctly. At early stages of the collision directed flow

of both kaons and antikaons is oriented in the direction of normal flow similar to that of nucleons [24]. Within the error bars there is no differences between $(K^+ + K^0)$ and $(K^- + \overline{K}^0)$. At this stage the matter is quite dense, mean free paths of particles are short, and similarities in kaon production and rescattering dominate over inequalities caused by different interaction cross-sections. It is worth mentioning that the directed flow of K and $\overline{K}$ is already sizable at $t = 3$ fm/c. This can be explained by a kick-off effect associated with the early stage of the collision, when the nuclei pass through each other. Later on the system becomes more dilute. For both kaons and antikaons the directed flow experiences significant transformations. Already at $t = 10$ fm/c the antiflow of antikaons starts to

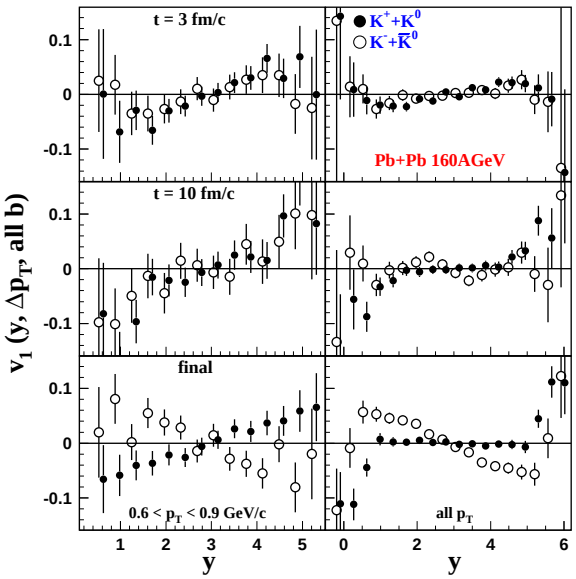

Figure 3. $v_1^K(y)$ (solid circles) and $v_1^{\bar{K}}(y)$ (open circles) in min. bias Pb+Pb collisions at SPS energy in high p_t interval $0.6 \leq p_t \leq 0.9$ GeV/c (left) and for all p_t (right panels) at times $t = 3$ fm/c, 10 fm/c, and final.

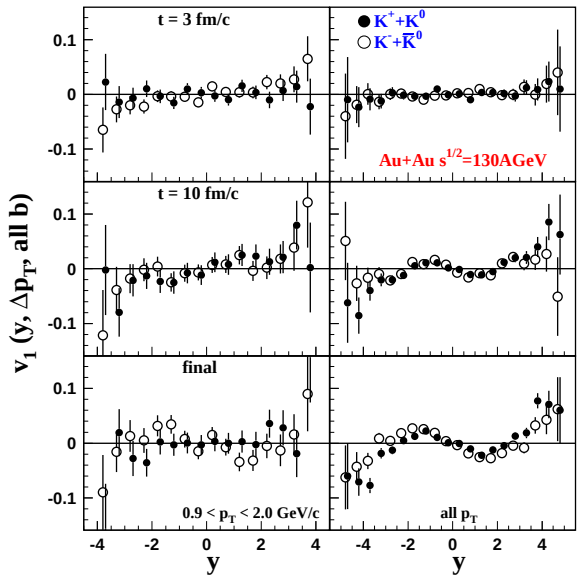

Figure 4. The same as Fig. 3 but for minimum bias Au+Au collisions at RHIC ($\sqrt{s} =$ 130 AGeV).

built up in the midrapidity range. Note, that $t = 10$ fm/c corresponds to the maximum of the kaon dN/dt distribution over their last elastic or inelastic interaction [34]. Here the differences in interaction cross sections and possible reaction mechanisms become crucial. Due to larger interaction cross-sections of K^- and $\overline{K}^0$ with other hadrons, the directed flow of these particles changes the orientation from a weak normal to strong antiflow. Even $(K^- + \overline{K}^0)$ with high transverse momentum demonstrate distinct antiflow, while the flow of $(K^+ + K^0)$ remains almost unchanged compared to that at $t = 10$ fm/c.

The directed flow of kaons and antikaons in minimum bias Au+Au collisions at $\sqrt{s} =$ 130 AGeV is displayed in Fig. 4 again at early stages, $t = 3$ fm/c and $t = 10$ fm/c, and at the final one, $t \geq 100$ fm/c. It is interesting that at $t = 3$ fm/c (i) the flow of $(K^+ + K^0)$ coincides within the statistical errors with the $(K^- + \overline{K}^0)$ flow, and (ii) the flow is generally very similar to that at the SPS energy at time $t = 3$ fm/c. Except of the target and projectile fragmentation region, where again the flow is probably produced by the initial kick, the kaon flow at this early stage of gold-gold collisions at RHIC energy

is isotropic with respect to the impact parameter axis. The spatial anisotropy in the distribution of baryonic charge seems to be unimportant at this stage. At $t = 10$ fm/c not only the directed flow of antikaons, but also that of kaons becomes antiflow-aligned at midrapidity. Similar behavior has been found within the RQMD model for the directed flow of nucleons at RHIC [31], suggesting that the nucleon directed flow is a side effect of the elliptic flow. The flow of produced particles, pions [31,35] and kaons [35], was found to be very flat at $|y| \leq 2$, in stark contrast to the QGSM predictions. We are awaiting the experimental data to resolve this problem.

4. ELLIPTIC FLOW

Rapidity and pseudorapidity distributions of elliptic flow of pions and charged particles at RHIC [15] are depicted in Fig. 5. For both energies elliptic flow displays strong in-plane alignment in accordance with the predictions of Ref. [5]. In the mid(pseudo)rapidity the flow is almost constant. It rises slightly at $|y|, |\eta| \approx 1.7$, and then drops with increasing rapidity. Pseudorapidity dependences of the elliptic flow of charged particles in the whole η

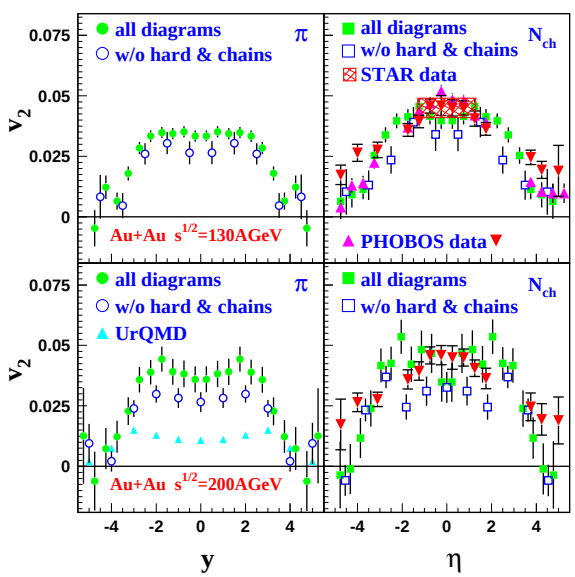

Figure 5. Rapidity dependence of elliptic flow of pions and charged particles at RHIC energies. See text for details.

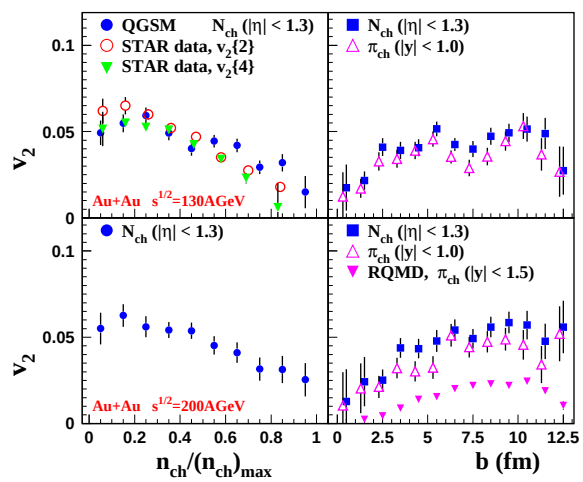

Figure 6. Centrality dependence of elliptic flow of pions and charged particles at RHIC energies.

range, which were obtained *before* the experimental data [15], are in a good agreement with the the results reported by PHOBOS Collaboration [36]. To elaborate on the influence of hard processes and multi-Pomeron exchanges on the elliptic flow formation the flow caused by the subprocesses without the hard and multichain contributions is also plotted in Fig. 5. It seems that in Au+Au collisions at $\sqrt{s} = 130A$ GeV the magnitude of the signal (except of the midrapidity range) can be reproduced without the many-string processes, although the particle multiplicity in the latter case is reduced by 30%. At $\sqrt{s} = 200A$ GeV their role becomes more significant, because the elliptic flow caused by other subprocesses cannot exceed the limit of 3−3.5% . Here it is important to stress

that the multichain diagrams alone, without rescattering, cannot affect the elliptic flow at all. The flow increases solely due to secondary interactions (absorption or rescattering) of produced particles in spatially asymmetric systems.

Figure 6 presents the centrality dependence of elliptic flow of charged particles. Since the centrality of events in the experiment [37] has been determined via the ratio of charged particle multiplicity to its maximum value $N_{ch}/(N_{ch})^{max}$, we compare the $v_2\,[N_{ch}/(N_{ch})^{max}]$ signal with the original impact parameter dependence $v_2(b)$. One can see that as a function of the impact parameter b elliptic flow is saturated at $b \approx 8$ fm for both energies, while as a function of the multiplicity ratio it increases nearly linearly with decreasing multiplicity up to $N_{ch}/(N_{ch})^{max} \approx 0.15$. The agreement with the STAR Collaboration data, obtained by 2-cumulant and 4-cumulant method [37,38], is good; similar results for the centrality dependence of v_2 were obtained also by the PHENIX Collaboration [39]. As expected, the flow in the midrapidity region is caused mainly by pions. The magnitude of the pionic flow in the QGSM calculations is twice as large as obtained, e.g. with RQMD [40]. Without many-string processes the QGSM is able to describe the flow only in central and semicentral collisions. It predicts a drop of the elliptic flow as the reaction becomes more peripheral, which is similar to the predictions of other string models. Note that neither the pseudorapidity nor the centrality dependence of the elliptic flow at RHIC is reproduced correctly so far by the hydrodynamic models.

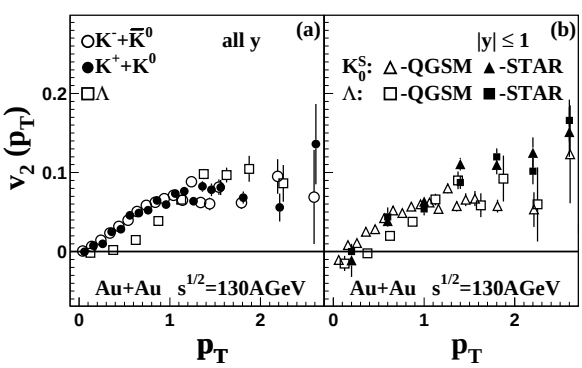

Figure 7. Transverse momentum dependence of the elliptic flow of strange particles in the whole rapidity (a) and in central rapidity interval (b) in minimum bias Au+Au collisions at RHIC. Data taken from [41].

Figure 7 depicts the p_T-dependence of the elliptic flow of strange hadrons at RHIC. The flow is close to zero for hadrons with $p_T \leq 0.25$ GeV/c, then rises linearly (kaons) up to $v_2^K(p_T) \approx 10\%$ within the interval $0.25 \leq p_T \leq 1.5$ GeV/c, and saturates at $p_T \geq 1.5\,$GeV/c in accord with the experimental data [41]. The flow of lambdas is weaker than the kaon flow at $p_T \leq 1.3$ GeV/c. At higher transverse momenta the situation is changed: here the Λ flow is stronger. This is the general trend in the p_T dependences of mesonic and baryonic flow at RHIC energies. The relative reduction of the elliptic flow within the interval $1 \leq p_T \leq 2$ GeV/c can be explained by the interplay between the flow of high-p_T particles, emitted at the onset of the collision, and the hydro-type flow of particles, which gained their transverse momentum in subsequent secondary interactions. Therefore, for proper understanding of the flow evolution it is very important to investigate the freeze-out picture of the hadrons.

5. FLOW AND FREEZE-OUT

The dN/dt distributions of n_{ch}, π, N, Λ, which are decoupled from the fireball after the last elastic or inelastic collision, are shown in Fig. 8. For the analysis ca. 20000 gold-gold

collisions with the impact parameter $b = 8$ fm at $\sqrt{s} = 130$ AGeV were simulated. One can see, that the particles are emitted during the whole course of the system evolution. In this respect the freeze-out picture obtained in microscopic model is different from the sharp freeze-out assumed in hydrodynamic models. Compared to AGS and SPS energies [34], a substantial part of hadrons leave the system immediately after their production within the first two fm/c. The pion distribution has a peak at $t = 5 - 6$ fm/c, while the distributions of baryons are wider due to the large number of rescatterings, which shift their dN/dt maxima to later times, $t = 10 - 12$ fm/c. Since the pion fraction dominates the other hadrons, the distribution of charged particles is similar to the pion one.

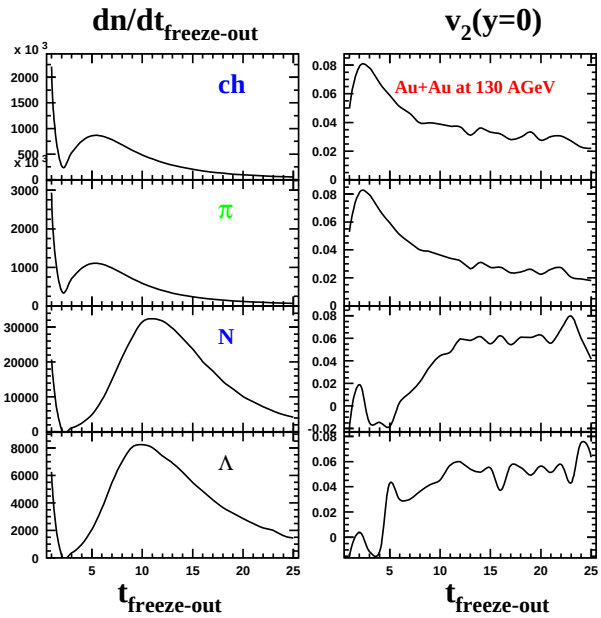

Figure 8. dN/dt distribution of n_{ch}, π, N, Λ over the time of their last interaction (left) and elliptic flow of these particles (right) for Au+Au collisions with $b = 8$ fm at $\sqrt{s} = 130$ AGeV.

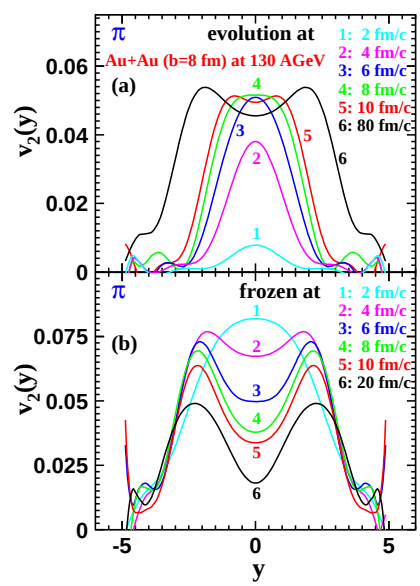

Figure 9. Gold-gold collisions with $b = 8$ fm at $\sqrt{s} = 130$ AGeV: (a) Snapshots of the v_2^π at 2, 4, ... 80 fm/c (from bottom to top), and (b) elliptic flow of pions already frozen at 2, 4, ... 20 fm/c (from top to bottom).

The elliptic flow carried by these species is presented in Fig. 8 as well. The baryonic and mesonic components are completely different: pions emitted from the surface of the expanding fireball within the first few fm/c carry the strongest flow, while later on the flow of pions is significantly reduced. In contrast to this, the baryon fraction acquires stronger elliptic flow during the subsequent rescatterings, thus developing the hydro-like flow. The saturation of the flow at the late stages can be explained by the lack of rescattering, since the expanding system becomes more dilute.

Finally, the time evolution of the elliptic flow of pions at midrapidity is studied. Two varieties of rapidity distribution are displayed in Fig. 9: elliptic flow of pions frozen at $t = 2$ fm/c, 4 fm/c, etc. till the late stages of the reaction; and the rapidity profile of the total pion elliptic flow at the same times. In the latter case, similarly to Sec. 3, the interactions were switched off, but resonances were allowed to decay. Here two observations should be mentioned. Firstly, although the elliptic flow at $y = 0$ reaches the maximum already at $t \approx$

6 fm/c, its formation is not over due to continuous freeze-out of particles. Secondly, there is no one-to-one correspondence between the apparent elliptic flow and the contribution to the final flow coming from the "survived" fraction of particles. For instance, apparent elliptic flow of pions at $t = 2$ fm/c is weak, but pions which are frozen at this moment have the strongest elliptic anisotropy caused by the absorption of the pion component in the squeeze-out direction.

6. CONCLUSIONS

In summary, the features of directed flow in the model can be stated as follows:
(i) wiggle structure of nucleon flow at midrapidity (SPS, RHIC);
(ii) the negative slope of the flow at $|y| \leq 2$ similar for all hadrons (RHIC);
(iii) normal flow of high-p_t hadrons at midrapidity (SPS, RHIC);
(iv) flows of kaons and antikaons are different at SPS but similar at RHIC.

Elliptic flow features at RHIC:
(i) flow at $\sqrt{s} = 200$ AGeV is only 10-15% stronger than that at $\sqrt{s} = 130$ AGeV;
(ii) $v_2(\eta)$ varies slightly within the interval $|\eta| \leq 2$ and quickly drops at $|\eta| > 2$;
(iii) $v_2(p_t)$ of mesons is stronger than the baryonic flow at $p_t \leq 1.5$ GeV/c but saturates earlier;
(iv) the time evolution of the mesonic flow is opposite to that of the baryonic one.
Many of these peculiarities are linked to different freeze-out pictures for baryons and mesons. In particular, it is shown that the flows of particles emitted at the beginning of the collision and during the course of the reaction are quite different. Therefore, phenomena such as collective flow and particle freeze-out should not be considered independently. The collective flow of hadrons appears to have a multi-component structure, caused by rescattering and absorption in a spatially anisotropic medium, which deserves further investigations.

Acknowledgments. Fruitful discussions with L. Csernai, R. Lacey, C.M. Ko, E. Shuryak, and N. Xu are gratefully acknowledged. This work was supported by the Deutsche Forschungsgemeinschaft, the Bundesministerium für Bildung und Forschung under contract 06TÜ986, and the Norwegian Research Council (NFR).

REFERENCES

1. Proc. of the Conf. Quark Matter'02 (Nantes, France, 2002) [Nucl. Phys. A 715 (2003) 1c].
2. W. Reisdorf and H.G. Ritter, Annu. Rev. Nucl. Part. Sci. 47 (1997) 663.
3. N. Herrmann, J.P. Wessels, and T. Wienold, Annu. Rev. Nucl. Part. Sci. 49 (1999) 581.
4. N. S. Amelin et al., Phys. Rev. Lett. 67 (1991) 1523.
5. J.-Y. Ollitrault, Phys. Rev. D 46 (1992) 229; Phys. Rev. D 48 (1993) 1132.
6. C.M. Hung and E.V. Shuryak, Phys. Rev. Lett. 75 (1995) 4003.
7. D.H. Rischke and M. Gyulassy, Nucl. Phys. A 597 (1996) 701.
8. L.V. Bravina, L.P. Csernai, P. Lévai, and D. Strottman, Phys. Rev. C 50 (1994) 2161; L.V. Bravina et al., Nucl. Phys. A 566 (1994) 461c.
9. L.V. Bravina, Phys. Lett. B 344 (1995) 49.
10. H. Sorge, Phys. Rev. Lett. 78 (1997) 2309; *ibid.* 82 (1999) 2048.
11. H. Heisenberg and A.-M. Levy, Phys. Rev. C 59 (1999) 2716.

12. L. P. Csernai and D. Röhrich, Phys. Lett. B 458 (1999) 454.
13. J. Brachmann et al., Phys. Rev. C 61 (2000) 024909.
14. P.F. Kolb, J. Sollfrank, and U. Heinz, Phys. Rev. C 62 (2000) 054909;
P.F. Kolb, P. Huovinen, U. Heinz, and H. Heiselberg, Phys. Lett. B 500 (2001) 232.
15. E.E. Zabrodin, C. Fuchs, L.V. Bravina, and A. Faessler, Phys. Lett. B 508 (2001) 184.
16. D. Teaney, J. Lauret, and E.V. Shuryak, Phys. Rev. Lett. 86 (2001) 4783.
17. V.K. Magas, L.P. Csernai, and D. Strottman, Nucl. Phys. A 712 (2002) 167.
18. Z.W. Lin and C.M. Ko, Phys. Rev. C 65 (2002) 034904.
19. D. Molnar and M. Gyulassy, Phys. Rev. C 62 (2002) 054907;
D. Molnar and S.A. Voloshin, nucl-th/0302014.
20. S. Voloshin and Y. Zhang, Z. Phys. C 70 (1996) 665.
21. A.M. Poskanzer and S.A. Voloshin, Phys. Rev. C 58 (1998) 1671.
22. H. Liu, S. Panitkin, and N. Xu, Phys. Rev. C 59 (1999) 348.
23. L.V. Bravina, A. Faessler, C. Fuchs, and E.E. Zabrodin, Phys. Rev. C 61 (2000) 064902;
Phys. Lett. B 470 (1999) 27.
24. E.E. Zabrodin, C. Fuchs, L.V. Bravina, and A. Faessler, Phys. Rev. C 63 (2001) 034902.
25. A.B. Kaidalov and K.A. Ter-Martirosian, Phys. Lett. B 117 (1982) 247;
A.B. Kaidalov, Surveys in High Energy Phys. 13 (1999) 265.
26. N.S. Amelin et al., Sov. J. Nucl. Phys. 50 (1989) 1058; Phys. Rev. C 47 (1993) 2299;
N.S. Amelin and L.V. Bravina, Sov. J. Nucl. Phys. 51 (1990) 211; *ibid.* 51 (1990) 133.
27. A. Capella, U. Sukhatme, C.I. Tan, and J. Tran Thanh Van, Phys. Rep. 236 (1994) 225.
28. K. Werner, Phys. Rep. 232 (1993) 87.
29. N.S. Amelin, E.F. Staubo, and L.P. Csernai, Phys. Rev. D 46 (1992) 4873.
30. V. Abramovskii, V. Gribov, and O. Kancheli, Sov. J. Nucl. Phys. 18 (1974) 308.
31. R.J.M. Snellings et al., Phys. Rev. Lett. 84 (2000) 2803.
32. A. Wetzler et al., NA49 Collaboration, Nucl. Phys. A 715 (2003) 583c;
C. Alt et al., NA49 Collaboration, Phys. Rev. C 68 (2003) 034903.
33. L.V. Bravina et al., J. Phys. G 28 (2002) 1977; Phys. Lett. B 543 (2002) 217.
34. L.V. Bravina et al., Phys. Lett. B 354 (1995) 196; Phys. Rev. C 60 (1999) 044905.
35. M. Bleicher and H. Stöcker, Phys. Lett. B 526 (2002) 309.
36. I. Park et al., PHOBOS Collaboration, Nucl. Phys. A 698 (2002) 564c;
S. Manly et al., PHOBOS Collaboration, Nucl. Phys. A 715 (2003) 614c.
37. K.H. Ackermann et al., STAR Collaboration, Phys. Rev. Lett. 86 (2001) 402.
38. R.J.M. Snellings, Star Collaboration, nucl-ex/0305001.
39. R.A. Lacey et al., PHENIX Collaboration, Nucl. Phys. A 698 (2002) 559c.
40. R.J.M. Snellings, A.M. Poskanzer, and S.A. Voloshin, nucl-ex/9904003.
41. P. Sorensen et al., STAR Collaboration, J. Phys. G 28 (2002) 2089.